

# Mechanical properties of Mg<sub>2</sub>Si thermoelectric materials with the addition of 0–4 vol% silicon carbide nanoparticles (SiC<sub>NP</sub>)

Robert D. Schmidt<sup>1,2</sup> · Xiaofeng Fan<sup>1</sup> · Eldon D. Case<sup>1</sup> · Patricia Bordon Sarac<sup>1</sup>

Received: 20 October 2014 / Accepted: 9 March 2015 / Published online: 17 March 2015  
© Springer Science+Business Media New York 2015

**Abstract** For thermoelectric generators, the individual thermoelectric elements are subjected to significant stresses under in-service conditions, due to thermal cycles, transients, and gradients, as well as thermal expansion mismatch and externally applied mechanical stresses. Most thermoelectric materials are brittle, possessing a low fracture toughness that is typically no more than 1.5 MPa m<sup>1/2</sup> and is often less than 0.5 MPa m<sup>1/2</sup>. The combination of the stresses encountered in the device application environment and the materials' low fracture toughness constitute a severe challenge to the viability of thermoelectric generators. The addition of silicon carbide nanoparticles (SiC<sub>NP</sub>) may provide a route to improving the fracture toughness for a wide range of thermoelectric materials. This study examines the mechanical properties, including elastic modulus, hardness, and fracture toughness for 0–4 vol% SiC<sub>NP</sub> incorporated into Mg<sub>2</sub>Si thermoelectric matrices.

## Background

Thermoelectric (TE) materials for solid state energy conversion have been extensively investigated in recent years, with the potential to recapture energy from waste heat sources. Typically, the efficiency of a TE material is measured by use of the dimensionless figure of merit,  $ZT$ ,

$$ZT = \frac{S^2 \sigma}{\kappa} T, \quad (1)$$

where  $S$  is the Seebeck coefficient,  $\sigma$  is the electrical conductivity,  $\kappa$  is the thermal conductivity, and  $T$  is temperature.

Thermoelectric generators, particularly when used in waste heat applications, are subjected to multiple sources of stress, including stresses due to thermal gradients, thermal shock, thermal expansion mismatch between materials, and externally applied stresses. Waste heat applications typically involve a heat source, such as exhaust from an engine. Automotive engines are typically run with several accelerations or decelerations, and the waste heat produced will likewise involve several thermal cycles during operation. The waste heat source therefore is a source with thermal transients, thermal shock, and thermal gradients, which produce stresses in the TE material. The elastic moduli are necessary to understanding the mechanical response to these stresses, including stresses that cause fracture and the calculation of fracture toughness.

In addition, stresses and flaws resulting from the manufacturing processes, such as scratches and surface microcracks during cutting or grinding, may result in fracture. Commonly, a TE material is machined into rectangular bar-shaped legs, with one hot surface of the leg and the opposite surface cold. A typical TE module has tens to hundreds of legs, all thermally in parallel, but electrically

---

✉ Robert D. Schmidt  
schmi402@egr.msu.edu

Xiaofeng Fan  
fanxiaof@msu.edu

Eldon D. Case  
casee@egr.msu.edu

Patricia Bordon Sarac  
patty\_bordonsarac@hotmail.com

<sup>1</sup> Chemical Engineering and Materials Science Department, Michigan State University, East Lansing, MI 48824, USA

<sup>2</sup> 428 S. Shaw Lane, Room 3264, East Lansing, MI, USA

in series, creating a condition where each leg is subjected to the full thermal cycle, but the failure in any one leg of the TE material electrically breaks the circuit and renders an entire module of a generator inoperable. Therefore, an understanding and control of the mechanical response and failure of the TE materials is critical to the reliable operation of a TE generator.

The fracture toughness,  $K_C$ , of thermoelectric materials is typically very low, less than  $1.5 \text{ MPa m}^{1/2}$ , and often less than  $0.5 \text{ MPa m}^{1/2}$  [1–4]. For comparison, window glass has a fracture toughness of about  $0.75 \text{ MPa m}^{1/2}$  [5]. Adding particles such as silicon carbide nanoparticles ( $\text{SiC}_{\text{NP}}$ ) may improve the fracture toughness for a wide range of TE materials.

More generally, fracture toughness may be increased by the incorporation of second phases, additions such as particles or whiskers, microstructural changes, or other mechanisms. For the purposes of this study, these may be grouped into extrinsic or intrinsic toughening mechanisms [6].

Extrinsic mechanisms (such as fiber or grain bridging, or crack stalling) work on the area behind the crack tip, applying some of the crack opening force to the sides of the crack and thereby reducing the amount of force acting at the crack tip [6, 7]. Crack stalling is a crack that has been arrested at one point, then reinitiates at another location. Extrinsic mechanisms may, for a few cycles, significantly improve fracture toughness. For example, in alumina, the addition of 20 % SiC whiskers increased  $K_C$  by a multiple of 3 [8], and additions of 20 and 40 % tetragonal zirconia increased  $K_C$  by a multiple of 3 and 5, respectively [8]. Similar increases were observed in glass and mullite [8].

These extrinsic toughening methods, however, are not desirable in a fatigue condition [6, 9–11] and can be destructive to the material [12–14]. Bridging across a crack by grains, whiskers, or fibers, for example, has been observed to be defeated by fatigue and can even be destructive in alumina [12, 15] and silicon [14]. When a bridge is defeated, the debris may fall into the crack and act as a wedge and extend the crack.

Intrinsic mechanisms (such as crack blunting or crack deflection) change the fracture toughness by acting on the area ahead of the crack tip, by distributing the load, changing the interface properties, or other methods to “increase the microstructural resistance” of the material [6]. With intrinsic toughening mechanisms, all of the force acting to open the crack acts only on the material around the crack tip. This difference has important implications in the potential for improving the fracture toughness overall, and specific implications for materials under fatigue conditions such as thermal cycling.

Intrinsic toughening mechanisms, including crack deflection, crack blunting, crack branching, or bowing, are

not defeated by thermal fatigue [6]. Therefore, intrinsic toughening mechanisms acting ahead of the crack tip are the desired type of toughening in fatigue [6, 10, 11] as would be the case for a TE device in waste heat recovery that is subjected to multiple thermal cycles.

The addition of nanoparticles can lead to intrinsic toughening. However, compared to large increases in  $K_C$  that are possible with extrinsic toughening, intrinsic toughening offers smaller but significant increases in  $K_C$  (Table 1). In alumina, additions of 5–20 % SiC nanoparticles increase the relative  $K_C$  by a factor of 1.16 [16, 17]. In  $\text{Bi}_2\text{Te}_3$ , a TE material, additions of 0.1–0.5 vol% SiC nanoparticles increased relative  $K_C$  by a factor of 1.18 [18].

$\text{Mg}_2\text{Si}$  may be used to examine several toughening mechanisms. Literature values of  $ZT$  show  $\text{Mg}_2\text{Si}$  to be a good TE material (Table 2), with  $ZT$  of 0.86 at 862 K for ( $\text{Mg}_2\text{Si}:\text{Bi} = 1:0.02$ ) [19] and 0.97 at 873 K for 0.5 at.% Sb-doped  $\text{Mg}_2\text{Si} + 5 \text{ wt}\% \text{ Ni}$  [20]. With values of  $ZT$  from 0.23 to 0.97 when doped with 2 % or less of dopant [19–24],  $\text{Mg}_2\text{Si}$  may be used as a suitable TE system to test additions of  $\text{SiC}_{\text{NP}}$ .

The addition of  $\text{SiC}_{\text{NP}}$  in TE materials may range from small influences on the  $ZT$  to improvements of up to 25 %, with the maximum increase in  $ZT$  typically due primarily to a reduction the thermal conductivity for quantities of less than 1 %  $\text{SiC}_{\text{NP}}$  addition. One study of  $\text{Bi}_2\text{Te}_3$  indicated an increase in  $ZT$  of 18 % for 0.1 vol%  $\text{SiC}_{\text{NP}}$  addition [25]; however, a follow-up study to refine the results indicated the maximum improvement in  $ZT$  was 5 % with 0.1 vol%  $\text{SiC}_{\text{NP}}$  [18]. In the similar TE material of  $\text{Bi}_{0.3}\text{Sb}_{1.7}\text{Te}_3$ , an increase in  $ZT$  of 8 % for 0.4 vol%  $\text{SiC}_{\text{NP}}$  addition was observed [26]. An examination of PbTe-based TE materials indicated a 25 % increase in  $ZT$  with 1 vol%  $\text{SiC}_{\text{NP}}$  addition, with no change for 0.1 or 2 vol% [27]. The improvements in  $ZT$  in  $\text{Bi}_2\text{Te}_3$ -based and PbTe-based TE materials also are accompanied by reductions in grain size, likely caused by inhibition of grain growth by  $\text{SiC}_{\text{NP}}$  [18, 26, 27], which may also explain some of the changes in  $ZT$ .

As reported on the MSDS for  $\text{Mg}_2\text{Si}$ , the material reacts with water [28], which requires handling without water or water-based solutions. However, this reaction is not a problem for crack growth and mechanical integrity when the material is handled in dry air [1]. Thus, the reaction between  $\text{Mg}_2\text{Si}$  and water will not influence the radial cracks from Vickers indentation used for examination of fracture properties [1].

The mechanical properties of the TE material must be understood first to determine the mechanical response to the stresses, as well as the potential for fracture, before it may be used in a design. Only with an understanding of the mechanical properties may a TE device be designed to properly withstand the thermal fatigue environment typical of many thermoelectric generator applications.

**Table 1** The fracture toughness,  $K_{IC}$ , has been improved in brittle materials, including the thermoelectric  $\text{Bi}_2\text{Te}_3$ , by the addition of SiC nanoparticles

Matrix material	$K_{IC}$ (MPa m <sup>1/2</sup> )	SiC addition (vol%)	$K_{IC}$ (MPa m <sup>1/2</sup> )	Relative change	Reference
$\text{Bi}_2\text{Te}_3$	1.14	0.1	1.35	1.18	[18]
		0.5	1.33	1.17	
		1.	1.19	1.04	
$\text{Al}_2\text{O}_3$	3.7–3.8 <sup>a</sup> 3.0–3.3 <sup>b</sup>	5 <sup>a</sup>	3.6	0.96 <sup>a</sup>	[16]
		20 <sup>a</sup>	3.4–3.6	0.93 <sup>a</sup>	
		5 <sup>b</sup>	3.6	1.14 <sup>b</sup>	
		20 <sup>b</sup>	3.5–3.7	1.14 <sup>b</sup>	
$\text{Al}_2\text{O}_3$	5.0 ± 0.3	5	5.4–5.6	1.10	[17]
		10	5.6–6.0	1.16	
		15	5.2–5.3	1.05	
		20	5.1–5.3	1.04	

<sup>a</sup> Specimen tested by single-edged notched beam

<sup>b</sup> Specimen tested by Vickers indentation

**Table 2** Doped  $\text{Mg}_2\text{Si}$ -based thermoelectric materials with  $ZT$  near 1 have been reported

Composition	Maximum $ZT$	Temperature for maximum $ZT$ (K)	Reference
$\text{Mg}_2\text{Si}:\text{Bi} = 1:0.02$	0.86	862	[19]
$\text{Mg}_2\text{Si}:\text{Sb} = 1:0.005 + 5 \text{ wt\% Ni}$	0.97	873	[20]
$\text{Mg}_2\text{Si}_{0.9}\text{Sn}_{0.1}:\text{Al} = 1:0.02$	0.68	864	[21]
$\text{Mg}_2\text{Si}:\text{Y} = 1:0.006$ (2000 ppm of Y)	0.23	600	[22]
$\text{Mg}_2\text{Si}:\text{Mg}_2\text{Pb} = 1:0.02$	0.56	873	[23]
$\text{Mg}_2\text{Si}:\text{Sb} = 1:0.02$	0.56	862	[24]

These reasonable  $ZT$  values for a thermoelectric material support the use of  $\text{Mg}_2\text{Si}$  as a reasonable thermoelectric system

## Experimental procedure

In this study, silicon carbide nanoparticles,  $\text{SiC}_{\text{NP}}$ , were added to  $\text{Mg}_2\text{Si}$  powders which were then processed to produce  $\text{Mg}_2\text{Si}-\text{SiC}_{\text{NP}}$  composites.

## Materials and specimen preparation

Powder was produced from lump  $\text{Mg}_2\text{Si}$  with 99.99 % metals basis purity (45518, 3–12 mm pieces, Alfa Aesar, Ward Hill MA), ground and sieved through a 53- $\mu\text{m}$  sieve, then milled by either (i) a planetary ball mill (PM) using an alumina-lined mill jar with 10-mm-diameter alumina grinding media at 150 RPM for 3 h, or (ii) a vibratory mill (VM) for 30 min with a WC lined jar, two 11.2-mm WC spheres and four 7.9-mm WC spheres, and a Viton gasket, sealed in the glove box with an additional layer of electrical tape. The electrical tape was wrapped around the VM jar lid for an additional seal between the mill jar body and lid as an added precaution against air leaking into the jar during milling. The PM-processed  $\text{Mg}_2\text{Si}$  powders were milled in an argon-filled glove box and the VM-processed powders were milled in a sealed, argon-filled jar. A previous analysis of the PM process on TE materials has

shown contamination of about 35 ppm or less using the same mill jar, media, and speeds [29].

Specimens were densified by pulsed electric current sintering (SPS Model 10-3, Thermal Technology LLC, Santa Rosa, CA) in a 12.7-mm-diameter graphite die. Sintering was performed at 800 °C and 50 MPa for 5 min, and with ramp rates of 100 °C/min and 45 MPa/min.

Specimen porosity was calculated based on a theoretical density of 2.12 g/cm<sup>3</sup> for the matrix  $\text{Mg}_2\text{Si}$  [1] and 3.21 g/cm<sup>3</sup> for the  $\text{SiC}_{\text{NP}}$  [30]. See [Starting material density, microstructure, and XRD](#) for details on the matrix density.

## Elasticity measurements

Elastic moduli were measured by resonant ultrasound spectroscopy (RUS). In RUS, the specimen is placed on a tripod of transducers. One transducer was swept through a range of frequencies and the mechanical resonance frequencies are picked up by the other two transducers. The resonances were fit to a model for the geometry, mass, and dimensions of the specimen to determine the elastic moduli. Additional details of the RUS procedure are provided elsewhere [4, 31, 32].

## Hardness and toughness measurements

Prior to indentation, each specimen was mounted with thermoplastic (CrystalBond 509, EMS, Hatfield, PA) onto an aluminum substrate, then polished with a series of diamond compounds with grit size from 35 to 1  $\mu\text{m}$ . Cleaning of the specimen between polishing grit sizes was performed by hand with ethanol rather than water to lessen any surface reaction between the  $\text{Mg}_2\text{Si}$  and water [28].

Hardness and fracture toughness for each of the specimens were measured by Vickers indentation, with loads of 1.96, 2.94, and 4.9 N and a dwell time of 5 s. Vickers hardness,  $H$ , is calculated by the equation,

$$H = \zeta \frac{1.8544F}{(2a)^2}, \quad (2)$$

where  $F$  is the indentation load,  $2a$  is the diagonal impression length, and  $\zeta$  is a correction factor, set at 0.95–0.97 based on indentations of a steel standard calibration block (Yamamoto Scientific Tools Lab Co. LTD, Chiba, Japan).

The fracture toughness,  $K_{\text{C}}$ , of a material may be estimated by measuring the radial crack length,  $c$ , of a Vickers indentation, by the equation,

$$K_{\text{C}} = \frac{\zeta(E/H)^{1/2}P}{c^{3/2}}, \quad (3)$$

where  $\zeta$  is a dimensionless constant, set as 0.016,  $E$  is the Young's modulus,  $H$  is the hardness, and  $P$  is the applied load [33].

## Microscopy

The specimens were examined by scanning electron microscope (SEM) at a working distance of either 8 or 15 mm and at an accelerating voltage of 15 kV (JEOL 6610LV or JSM-7500F, JEOL Ltd., Japan). The average grain size (GS) of each of the sintered specimens was determined using the linear intercept procedure (ASTM E112) with a minimum of 200 intercepts per image and a stereographic projection factor of 1.5 [34]. Surface details were examined with secondary electron imaging (SEI) and elemental contrasts were examined by backscatter electron imaging (BEI).

## Results and discussion

### Microstructural analysis

Prior to sintering, both the PM and the VM powders were examined for size range and morphology. For the PM powder, there was a wide distribution from sub-micron

particles to 5- $\mu\text{m}$  particles or greater, average particle size by BET was 0.7  $\mu\text{m}$  (Fig. 1).

To incorporate  $\text{SiC}_{\text{NP}}$  with a vendor-specified average particle size of 45–55 nm (44646, Lot number E15T018, Alfa Aesar) into the PM powder, the PM-milled  $\text{Mg}_2\text{Si}$  and  $\text{SiC}_{\text{NP}}$  were planetary ball milled at 120 RPM for 3 h in an argon-filled glove box with the same mill jar and media used to mill the  $\text{Mg}_2\text{Si}$  powder.

For the VM powder, the particle size was relatively uniformly distributed with diameters of 0.2–2  $\mu\text{m}$  (Fig. 2). The  $\text{SiC}_{\text{NP}}$ , with impurities of <0.15 % Si, <0.15 % Cl, <0.75 % C, and <1.25 % O, (44646, Lot number E15T018, Alfa Aesar) were incorporated into the VM powder simultaneously with milling the sieved powder.

The original PM powder average particle size of 0.7  $\mu\text{m}$  (Fig. 1) was smaller than the average GS of the sintered PM specimens of 2.0–3.9  $\mu\text{m}$  (Table 3), indicating some grain growth during sintering (Fig. 3a–c).

No BET particle size measurement was performed on the VM powder to compare the powder particle size to GS. However, the average GS of the VM specimens is 0.4–0.8  $\mu\text{m}$  (Table 3; Fig. 3d), which is consistent with only limited grain growth, as determined from the SEM micrographs of the VM powder (Fig. 2).

### Starting material density, microstructure, and XRD

All sintered specimens in this study except one have a density of 2.00–2.06  $\text{g}/\text{cm}^3$ . The one specimen with a density of 1.93  $\text{g}/\text{cm}^3$ , VM-0SiC-02, is mentioned individually, but any averages or trends in mechanical properties excluded VM-0SiC-02 as an outlier.

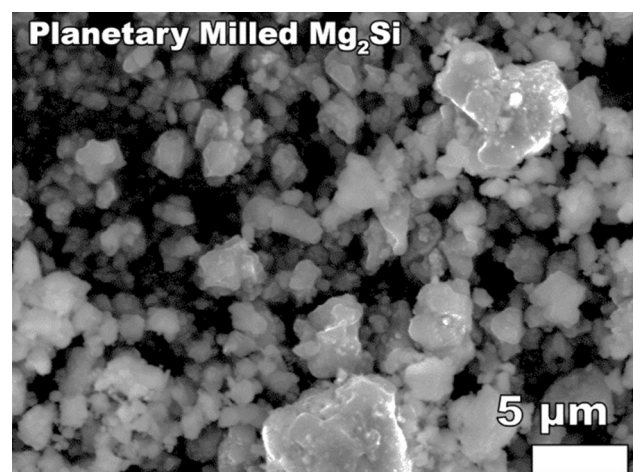


**Fig. 1** Planetary-milled  $\text{Mg}_2\text{Si}$  powder exhibited typical particle sizes of sub-micron to 5  $\mu\text{m}$  in SEM. The powder has a surface area of 4.4  $\text{m}^2/\text{g}$  measured by BET, or approximately 0.7  $\mu\text{m}$  average particle size

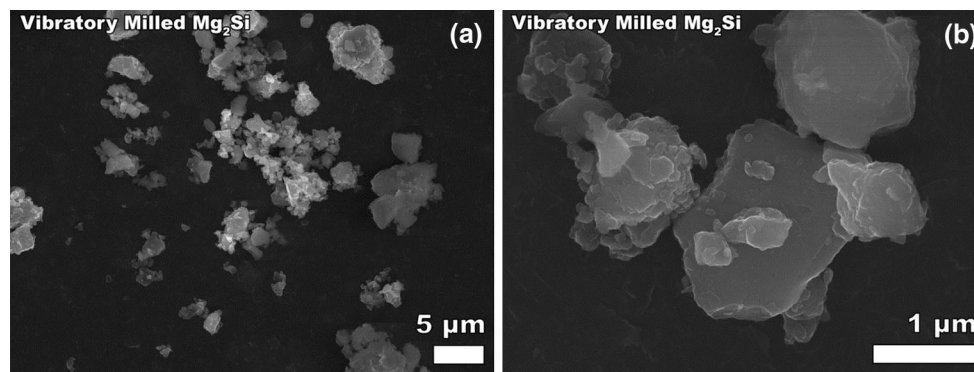


**Fig. 2** Vibratory-milled  $\text{Mg}_2\text{Si}$  powder exhibited typical particle sizes of 0.2–2  $\mu\text{m}$  in SEM. Note the VM powder often formed agglomerates of  $\sim 5 \mu\text{m}$

**Table 3** Specimens in this study were either milled by planetary ball mill (PM) or vibratory mill (VM), with up to 4 vol%  $\text{SiC}_{\text{NP}}$  additions, then sintered by pulsed electric current sintering to produce specimens with a density ( $\rho$ ) of 2.00  $\text{g}/\text{cm}^3$  or greater for all specimens except VM-0SiC-2

Specimen	$\text{SiC}_{\text{NP}}$ vol% addition	$\rho$ ( $\text{g}/\text{cm}^3$ )	GS ( $\mu\text{m}$ )
PM-0SiC	0.0	2.03	2.4
PM-0.5SiC	0.5	2.02	2.0
PM-1SiC	1.0	2.02	2.0
PM-1.5SiC	1.5	2.01	2.1
PM-2SiC	2.0	2.06	1.3
PM-3SiC	3.0	2.04	3.9
PM-4SiC	4.0	2.02	3.6
VM-0SiC-1	0.0	2.00	0.6
VM-0SiC-2	0.0	1.93	0.4
VM-0.5SiC	0.5	2.01	0.6
VM-1SiC	1.0	2.03	0.7
VM-1.5SiC	1.5	2.03	0.8
VM-2SiC	2.0	2.03	0.6

The average grain sizes (GS) by the linear intercept method are a function of the milling method, and not a function of  $\text{SiC}_{\text{NP}}$  additions

Most of the sintered specimen densities are higher than theoretical density for  $\text{Mg}_2\text{Si}$  of 2.00  $\text{g}/\text{cm}^3$  reported in the literature [35]. The higher density is because of the presence of MgO within the material. The starting material as received from the vendor has been shown to contain approximately 8 vol% of MgO, with a density of 3.58  $\text{g}/\text{cm}^3$  [36], and likely to have a composite theoretical density near 2.12  $\text{g}/\text{cm}^3$  [1] (see [Elasticity results](#)). The presence of MgO was confirmed by XRD for specimens PM-0SiC and VM-0SiC-1 (Fig. 4) at concentrations between 5 and 10 %. No other phases were observed in XRD. The measured lattice parameter of the  $\text{Mg}_2\text{Si}$  from XRD was  $0.6350 \pm 0.0004$  nm for BM-0SiC and  $0.6353 \pm 0.0003$  nm for VM-0SiC-1. The lattice parameter of MgO was  $0.4208 \pm 0.0003$  nm and  $0.4209 \pm 0.0002$  nm, respectively.

Assuming no vacancies or interstitials, the theoretical density of  $\text{Mg}_2\text{Si}$  from XRD is 1.99 and 3.59  $\text{g}/\text{cm}^3$  for MgO, consistent with the accepted density in the literature of 2.00  $\text{g}/\text{cm}^3$  for  $\text{Mg}_2\text{Si}$  [35] and of 3.58  $\text{g}/\text{cm}^3$  for MgO [36]. The XRD results are consistent with a matrix material consisting of 92 %  $\text{Mg}_2\text{Si}$  and 8 % MgO (Fig. 4), with mass density of 2.12  $\text{g}/\text{cm}^3$  [1]. For this study, the porosity of the materials was therefore calculated from a density of 2.12  $\text{g}/\text{cm}^3$  for the matrix and 3.21  $\text{g}/\text{cm}^3$  for the  $\text{SiC}_{\text{NP}}$  [30].

Previous examination has shown that the as-received SiC nanopowder from two vendors (Alfa Aesar and Nanostructured & Amorphous Materials Inc.) consists primarily of particles, approximately 50 nm in diameter, agglomerated into clusters of 100 nm to 20  $\mu\text{m}$  in diameter [37]. These agglomerates do not appreciably break apart with milling [37]. In this study, the  $\text{SiC}_{\text{NP}}$  material was the same catalog number and lot from one of the two previously examined vendors (44646, Lot number E15T018, Alfa Aesar).

## Elasticity results

The elasticity for specimens with  $\text{SiC}_{\text{NP}}$ , excluding the outlier specimen VM-0SiC-02 with density of 1.93  $\text{g}/\text{cm}^3$ , was not a function of  $\text{SiC}_{\text{NP}}$  addition up to 4 vol%, nor powder processing methodology (Fig. 5, Table 4). The average Young's modulus,  $E$ , for the PM specimens with 0–4 vol%  $\text{SiC}_{\text{NP}}$  was  $113.3 \pm 4.0$  and  $111.1 \pm 2.3$  GPa for VM specimens (Fig. 5a, b). The small variations in elastic moduli were not observed to be a function of the  $\text{SiC}_{\text{NP}}$  addition (Fig. 5), rather a function of the limited differences in porosity among specimens (Fig. 6).

### Elasticity and $\text{SiC}_{\text{NP}}$ addition

If the  $\text{SiC}_{\text{NP}}$  addition does not react with the  $\text{Mg}_2\text{Si}$  matrix, the elastic modulus of the composite material with addition

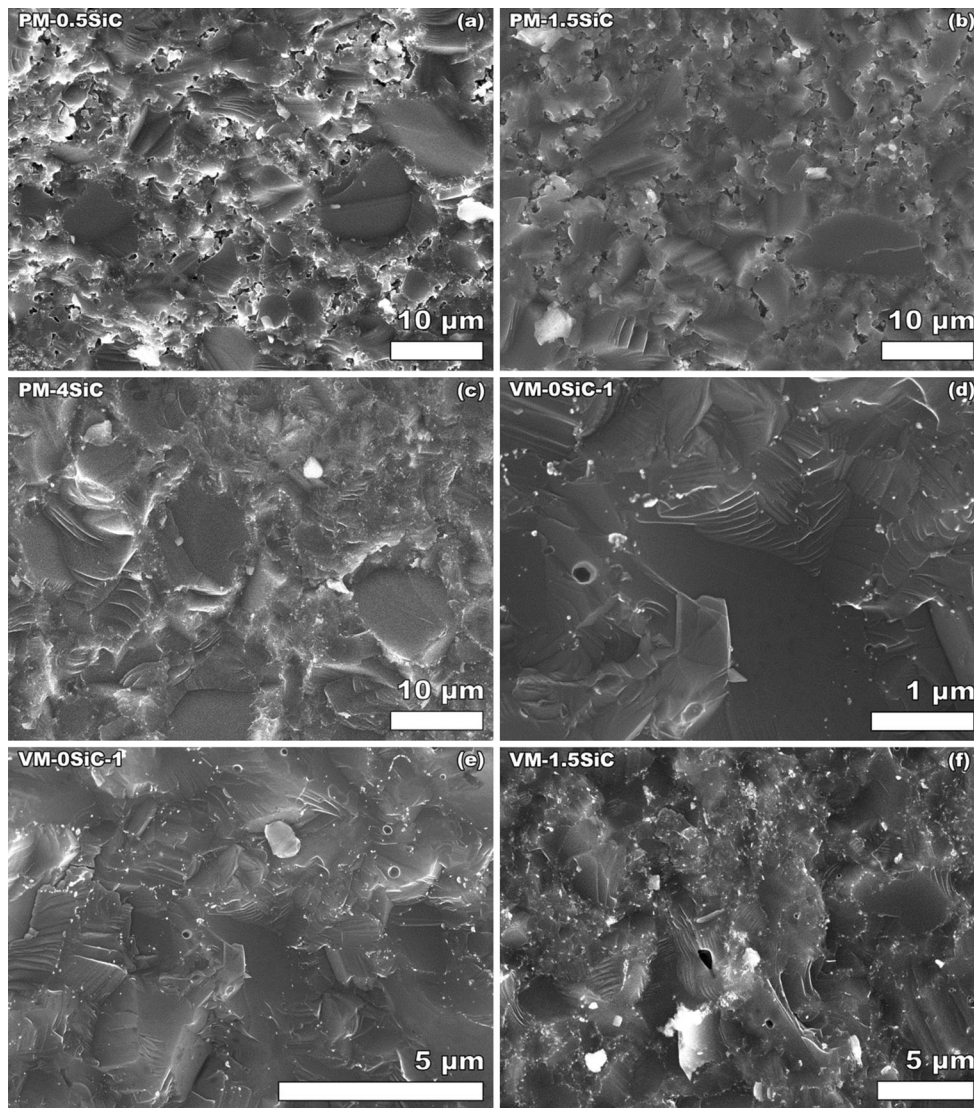


**Fig. 3** For Mg<sub>2</sub>Si fracture surfaces, trans-granular fracture dominates in all specimens. The PM specimens (a–c) with varying amounts of SiC<sub>NP</sub> addition did not show any appreciable difference in grain size, although changing to VM processing significantly reduced the grain

size (d–f). Note the difference in scale between the PM images (a–c) and the VM images (d–f). The SiC<sub>NP</sub> additions are not apparent in the fracture surface images

of up to 4 vol% SiC<sub>NP</sub> may be modeled as a mixture of two independent materials. In a study of SnTe with 0–4 vol% SiC<sub>NP</sub> addition [37], the Hashin model [38–40] described relatively well the resulting change in Young’s modulus, written as

$$E_c = E_m \left( \frac{E_m V_m + E_r \{V_r + 1\}}{E_r V_m + E_m \{V_r + 1\}} \right), \tag{4}$$

where  $E_c$  is the Young’s modulus of the composite,  $E_m$  is the Young’s modulus of the matrix material,  $E_r$  is the Young’s modulus of the reinforcing phase, and  $V_m$  and  $V_r$  are the volume fraction of the matrix and the reinforcing phase, respectively. Applying the Hashin model (Eq. (4)) to the materials in this study, using  $E_r$  of 450 GPa from the

Young’s modulus of the reinforcing phase SiC<sub>NP</sub> [30, 41] and  $E_m$  of 112 GPa from the Mg<sub>2</sub>Si measured in this study, the calculated  $E_c$  for the composite with 4 vol% SiC<sub>NP</sub> is 117.5 GPa, which is similar to the measured  $E$  of  $114.5 \pm 0.6$  GPa for specimen PM-4SiC (Fig. 5a).

*Elasticity and porosity*

Small variations in density of the specimens, from 2.00 to 2.06 g/cm<sup>3</sup>, is likely the dominant source of variation in  $E$  measured in this study (Figs. 5a, b, 6). Typically, for small variations in porosity,  $P$ , the change in  $E$  may be modeled by the empirical equation,

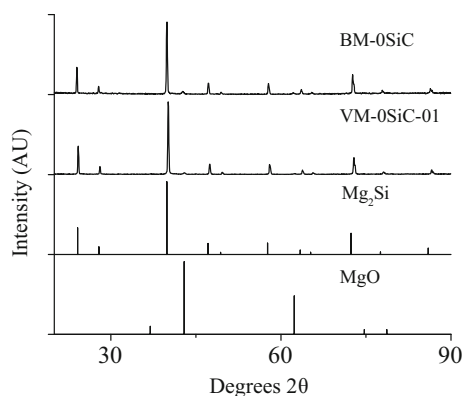


**Fig. 4** X-ray diffraction from the PM-0SiC and VM-0SiC-1 specimens indicates primarily  $\text{Mg}_2\text{Si}$  phase, with an impurity of 5–10 % MgO detected

$$E = E_0(1 - b_E P), \quad (5)$$

where  $E_0$  is the Young's modulus of a fully dense material and  $b_E$  is a material-dependent constant, typically between 2 and 6 for a wide range of materials [42]. Assuming the matrix material contains 8 % MgO [1] (density  $3.58 \text{ g/cm}^3$  [43, 44]) and 92 %  $\text{Mg}_2\text{Si}$  (density  $2.00 \text{ g/cm}^3$  [35]), the composite theoretical densities (matrix density,  $2.126 \text{ g/cm}^3$ ,  $\text{SiC}_{\text{NP}}$  density,  $3.16 \text{ g/cm}^3$  [28]) were calculated. The volume fraction porosity,  $P$ , was calculated for the composite materials. The  $E$  versus  $P$  for the full set of 13

composite specimens in this study were fit to Eq. (5), with the  $b_E$  was  $3.5 \pm 0.5$  and the  $E_0$  was  $138 \pm 5 \text{ GPa}$  (Fig. 6). The linear relationship indicates that the  $E$  for the 14 specimens is a function of  $P$  (Fig. 6). The error on the  $E_0$  and  $b_E$  is relatively large, likely because of the restricted range of  $P$  for the specimens this study.

The experimentally determined value of  $E$  ranged from 116.9 to 117.7 GPa for a previous study of  $\text{Mg}_2\text{Si}$  from lump material purchased from the same vendor and processed by PM [1] (Table 4). The small ( $\sim 4 \%$ ) difference in elastic moduli between this study and the previous study is likely due to the slightly higher density specimens in the previous study, 2.07–2.09  $\text{g/cm}^3$  (Table 4).

#### Literature comparison of elasticity

The matrix material in this study is itself a composite of  $\text{Mg}_2\text{Si}$  and approximately 8 % MgO (Fig. 4) [1]. As with the  $\text{SiC}_{\text{NP}}$  addition, the moduli of the composite may be modeled from the moduli of the constituent materials,  $\text{Mg}_2\text{Si}$  and MgO.

The elastic moduli of single crystals of  $\text{Mg}_2\text{Si}$  and MgO are available in the literature [35, 36]. For a given material, the single crystal moduli may be used to calculate the mean of the Hashin and Shtrikman bounds,  $\langle \text{H-S} \rangle$ , which give the aggregate average moduli of the material. The aggregate average moduli in turn correspond to the elastic

**Fig. 5** The Young's modulus (a, b) and shear modulus (c, d) of  $\text{Mg}_2\text{Si}$  varied primarily due to small variations in density. The variation in vol%  $\text{SiC}_{\text{NP}}$  did not significantly affect the moduli, regardless of if the specimens were planetary milled (a, c) or vibratory milled (b, d). The solid lines represent the average and dashed lines represent one standard deviation from average

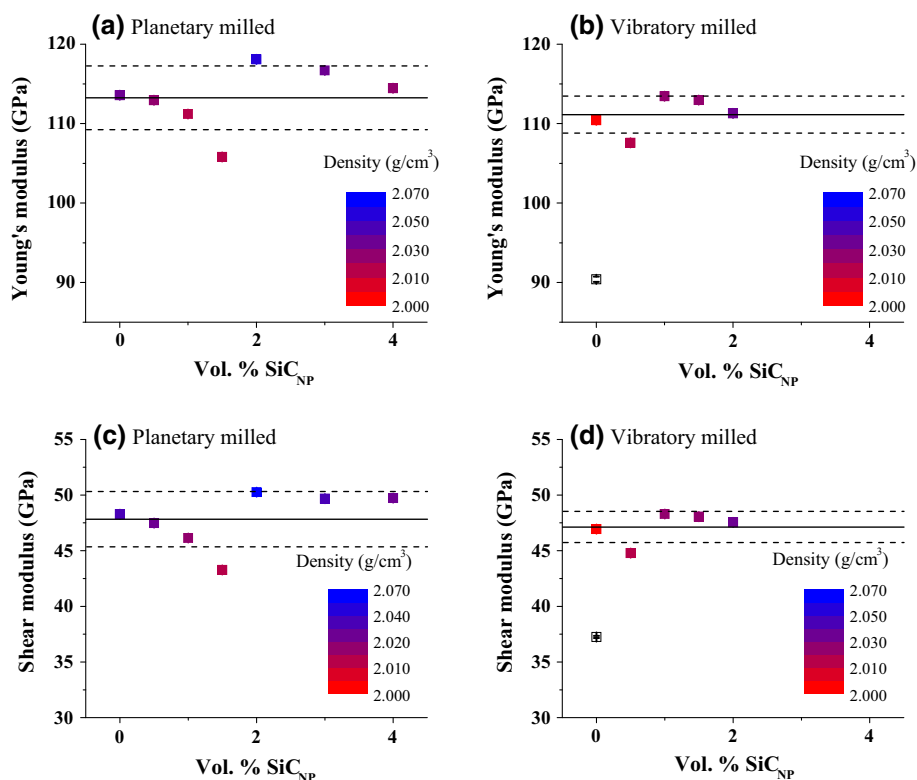


**Table 4** The Young’s modulus,  $E$ , shear modulus,  $G$ , density,  $\rho$ , and volume fraction porosity,  $P$ , for the specimens in this study, as compared to the range of  $E$ ,  $G$ , and  $\rho$  in a previous study on three  $Mg_2Si$  specimens produced by the same vendor

Specimen	$E$ (MPa)	$G$ (MPa)	$\rho$ (g/cm <sup>3</sup> )	$P$	Reference
PM-0SiC	113.6 ± 0.3	48.3 ± 0.1	2.03	0.044	This study
PM-0.5SiC	112.9 ± 0.3	47.5 ± 0.1	2.02	0.051	This study
PM-1SiC	111.2 ± 0.3	46.1 ± 0.1	2.02	0.055	This study
PM-1.5SiC	105.8 ± 0.4	43.3 ± 0.1	2.01	0.061	This study
PM-2SiC	118.1 ± 0.2	50.3 ± 0.1	2.06	0.039	This study
PM-3SiC	116.7 ± 0.2	49.7 ± 0.1	2.04	0.056	This study
PM-4SiC	114.5 ± 0.6	49.7 ± 0.2	2.02	0.068	This study
VM-0SiC-1	110.4 ± 0.2	46.9 ± 0.1	2.00	0.058	This study
VM-0SiC-2	90.4 ± 0.3	37.3 ± 0.1	1.93	0.090	This study
VM-0.5SiC	107.6 ± 0.4	44.7 ± 0.1	2.01	0.057	This study
VM-1SiC	113.4 ± 0.2	48.3 ± 0.1	2.03	0.052	This study
VM-1.5SiC	113.0 ± 0.2	48.1 ± 0.1	2.03	0.054	This study
VM-2SiC	111.3 ± 0.3	47.5 ± 0.1	2.03	0.053	This study
$Mg_2Si$	116.9–117.7	48.92–50.09	2.07–2.09	0.014–0.024	[1]

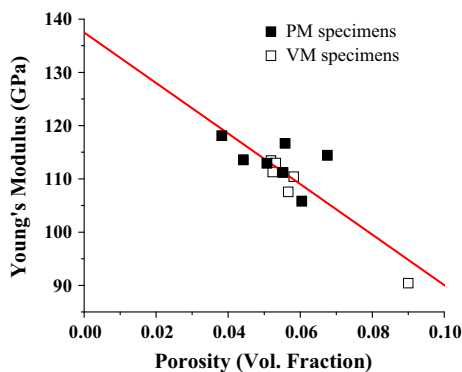


**Fig. 6** The Young’s modulus,  $E$ , decreases linearly with porosity for the set of 13 specimens in this study

moduli for a polycrystalline specimen composed of randomly oriented crystallites [45]. The mean of the Hashin and Shtrikman bounds,  $\langle H-S \rangle$ , are  $E = 303$  GPa for  $MgO$  [36] and  $E = 110.9$  for  $Mg_2Si$  [35]. Using the Hashin composite model (Eq. 4) with the  $\langle H-S \rangle$  moduli for  $MgO$  and  $Mg_2Si$  yields a prediction of  $E = 119.5$  GPa for a fully dense composite of  $Mg_2Si$  with 8 %  $MgO$ .

To compare this literature-based value of  $E$  with the specimens in this study, the porosity must also be considered. In this study, the specimen PM-0SiC with  $P = 0.044$  (Table 4) may be used as a point of comparison since it has no SiC nanoparticle addition. In order to use Eq. (5) to estimate the decrement in elastic modulus due to porosity, a value of the material-dependent constant  $b_E$  is needed but since no value of  $b_E$  is available in the literature for  $Mg_2Si$ , we estimated a range for  $b_E$  based on the experimentally determined  $b_E$  values of two other TE materials, namely  $b_E = 2.34$  for  $YbAl_3$  [46] and  $b_E = 3.5$  for lead–antimony–silver–tellurium (LAST) [47]. Using Eq. (5) with

$E_0 = 119.5$  GPa,  $P = 0.044$  and  $b_E$  values of 2.34 and 3.5, the  $E$  range based on literature values is from 101.1 to 107.2 GPa. The  $E$  of PM-0SiC in this study,  $113.6 \pm 0.3$  GPa (Table 4), is reasonably close to the calculated  $E$  range based on literature values.

### Hardness and toughness results

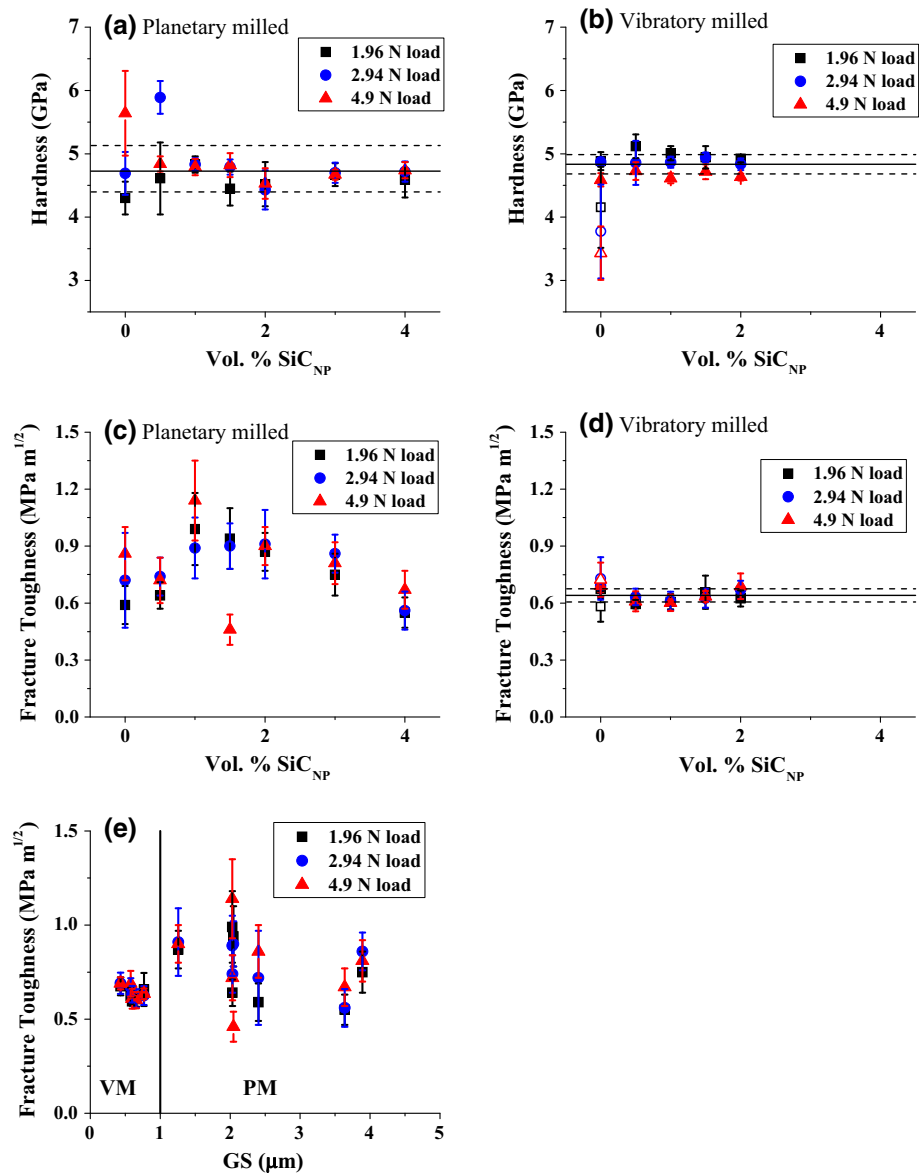
Hardness,  $H$ , by Vickers indentation for specimens with  $SiC_{NP}$ , excluding one outlier, was relatively insensitive to vol%  $SiC_{NP}$ , from 0 % to 4 vol%  $SiC_{NP}$ , indentation load, from 1.96 to 4.9 N, or powder processing technique, averaging  $4.76 \pm 0.37$  GPa for the PM specimens (Fig. 7a), and  $4.83 \pm 0.15$  GPa for the VM specimens (Fig. 7b). The outlier is specimen VM-0SiC-02 with a density of 1.93 g/cm<sup>3</sup>, lower than the 2.00–2.06 g/cm<sup>3</sup> density of the other 12 specimens in this study. The  $H$  of the outlier VM-0SiC-02 specimen is indicated by the open symbol in Fig. 7b.

The fracture toughness,  $K_C$ , is dependent on the powder processing conditions. The  $K_C$  of the PM composite reached a maximum at 1 vol%  $SiC_{NP}$ , an increase of about 33 % over the unreinforced PM material, and is relatively insensitive to  $SiC_{NP}$  addition between 1 and 2 vol%  $SiC_{NP}$  additions (Fig. 7c). In contrast, the VM composite material was relatively insensitive to any additions of up to 2 vol%  $SiC_{NP}$  (Fig. 7d). The VM material also exhibited a much smaller variation in measured  $K_C$ , with the coefficient of variation, CV, averaging 0.08 and ranging from 0.04 to 0.14 (Fig. 7d). The CV of the PM material averages 0.16 and ranging from 0.11 to 0.34.

The length of radial cracks,  $c$ , from a set of Vickers indentations were used to calculate fracture toughness,  $K_C$ , (Eq. 3). A more consistent radial crack length measurement was observed in the VM specimens relative to the PM specimens, resulting in a smaller CV observed for  $K_C$



**Fig. 7** The hardness, (a) and (b), is not a function of the milling procedure or the vol% SiC<sub>NP</sub>, but less scatter was observed in the (b) vibratory-milled specimens than the (a) planetary ball-milled specimens. The fracture toughness exhibited a maximum at 1 vol% SiC<sub>NP</sub> for the (c) planetary ball-milled specimens, but the fracture toughness is not a function of vol% SiC<sub>NP</sub> for the (d) vibratory-milled specimens. Furthermore, fracture toughness is not a function of grain size, regardless of milling (e). *Open symbols* in (b, d), and e indicate a specimen with lower density of 1.93 g/cm<sup>3</sup>, relative to the 2.00–2.06 g/cm<sup>3</sup> for all other specimens in this study. The *solid lines* represent the average and *dashed lines* represent one standard deviation from average



calculated from the radial crack lengths. The smaller CV in the VM specimens may be related to the smaller GS of the VM specimens, relative to the PM specimens. The smaller CV is particularly important when considering the distribution of strength, and the related probability of failure at a given load. Assuming fracture occurs from a critical flaw, fracture strength,  $\sigma_{STR}$ , and fracture toughness are related by the equation,

$$\sigma_{STR} = YK_C / (\pi a)^{1/2}, \quad (6)$$

where  $a$  is the flaw size from which the crack originates, and  $Y$  is a shape factor for the flaw [33]. From Eq. (6), a larger variation in  $K_C$  results in a larger variation in  $\sigma_{STR}$ .

The average measured strength is higher than the strength that may be safely used in design, and the smaller CV for the strength values in the VM specimens indicates a

lower probability of failure at a load less than the average strength [33]. Thus, a smaller scatter of strength for VM specimens than PM specimens indicates a lower likelihood of failure for a given load, and a smaller safety margin may be required for reliable use of the VM material.

In this study,  $K_C$  is not a function of GS for the Mg<sub>2</sub>Si with no SiC<sub>NP</sub> addition (Fig. 7c, d). This result is expected for cubic materials such as Mg<sub>2</sub>Si, because  $K_C$  is largely independent of GS [33], and specifically for Vickers indentation crack length, “there should be a rather weak dependence of crack length on GS” [33].

However, the effect of SiC<sub>NP</sub> addition on  $K_C$  was influenced by the powder processing technique. The difference in size between the added SiC<sub>NP</sub> particles and the Mg<sub>2</sub>Si matrix may play a role in the behavior of  $K_C$ . In a study on fracture toughness on TE material specimens

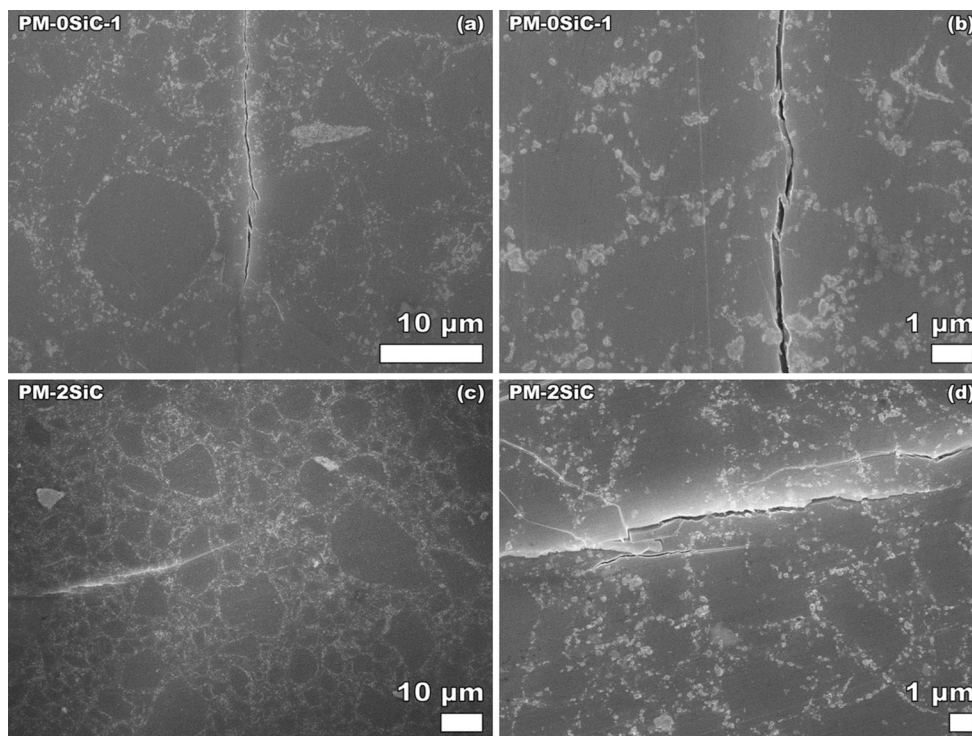


**Fig. 8** Crack bridging in PM  $\text{Mg}_2\text{Si}$  was commonly observed in radial cracks for all the  $\text{Mg}_2\text{Si}$  specimens in this study

sintered from a blend of nanoparticles with microparticles of the same composition,  $\text{Co}_4\text{Sb}_{11.5}\text{Te}_{0.5}$ , the  $K_C$  increased with additions of nanoparticles [42]. Similar to the  $K_C$  of  $\text{Co}_4\text{Sb}_{11.5}\text{Te}_{0.5}$  [42], this study indicates that the toughening due to addition of  $\text{SiC}_{\text{NP}}$  may depend on GS of the matrix  $\text{Mg}_2\text{Si}$  relative to the  $\text{SiC}_{\text{NP}}$ .

The polished and indented surface micrographs of the PM specimens (Fig. 8) and VM specimens (Fig. 9) exhibit some brighter contrast areas of MgO particles, primarily at the grain boundaries. These MgO particles are more pronounced in the PM specimens (Fig. 8b, d) than in the VM specimens (Fig. 9b, d). The XRD results indicate a similar content of MgO in the specimens processed by either PM or VM (Fig. 4), indicating that the VM process has dispersed the MgO particles more uniformly within the matrix. The dispersion of the MgO particles within the matrix may be related to the fracture mode observed on the fracture surfaces.

The fracture surfaces of the PM specimens exhibit mixed fracture modes of trans-granular and inter-granular fracture (Fig. 3a–c), while the fracture surfaces of the VM specimens exhibit primarily trans-granular fracture. The inter-granular fracture mode is associated with a crack deflection mechanism during fracture. Toughening by  $\text{SiC}_{\text{NP}}$  additions was only observed in the PM specimens (Fig. 7c) with the mixed fracture modes observed. The different toughening behavior of  $\text{SiC}_{\text{NP}}$  additions in the PM

and the VM specimens suggests that the toughening provided by the  $\text{SiC}_{\text{NP}}$  in the PM specimens with 1–2 vol%  $\text{SiC}_{\text{NP}}$  additions may be related to the crack deflection mechanism.

#### *Crack bridging and toughness*

Crack bridging and stalling were observed on all of the different  $\text{Mg}_2\text{Si}$  specimens, both with and without  $\text{SiC}_{\text{NP}}$  additions and regardless of processing by PM (Fig. 8) or VM (Fig. 9). Both bridging and stalling are extrinsic toughening mechanisms, and not beneficial to  $K_C$  in a fatigue loading condition such as thermal cycling [9, 12]. In some cases, bridging or stalling may be controlled through grain size reduction. Bridging in monophase alumina material was eliminated by reducing the GS [12], although changing the powder processing of the  $\text{Mg}_2\text{Si}$  in this study did not produce a similar result.

## Conclusions

The Young's modulus,  $E$ , of  $\text{Mg}_2\text{Si}$  was not observed to be a function of the  $\text{SiC}_{\text{NP}}$  addition or milling condition, but rather a function of the limited differences in porosity among specimens, and averaged 112 GPa. Hardness,  $H$ , was insensitive to 0 %–4 vol%  $\text{SiC}_{\text{NP}}$  addition, indentation

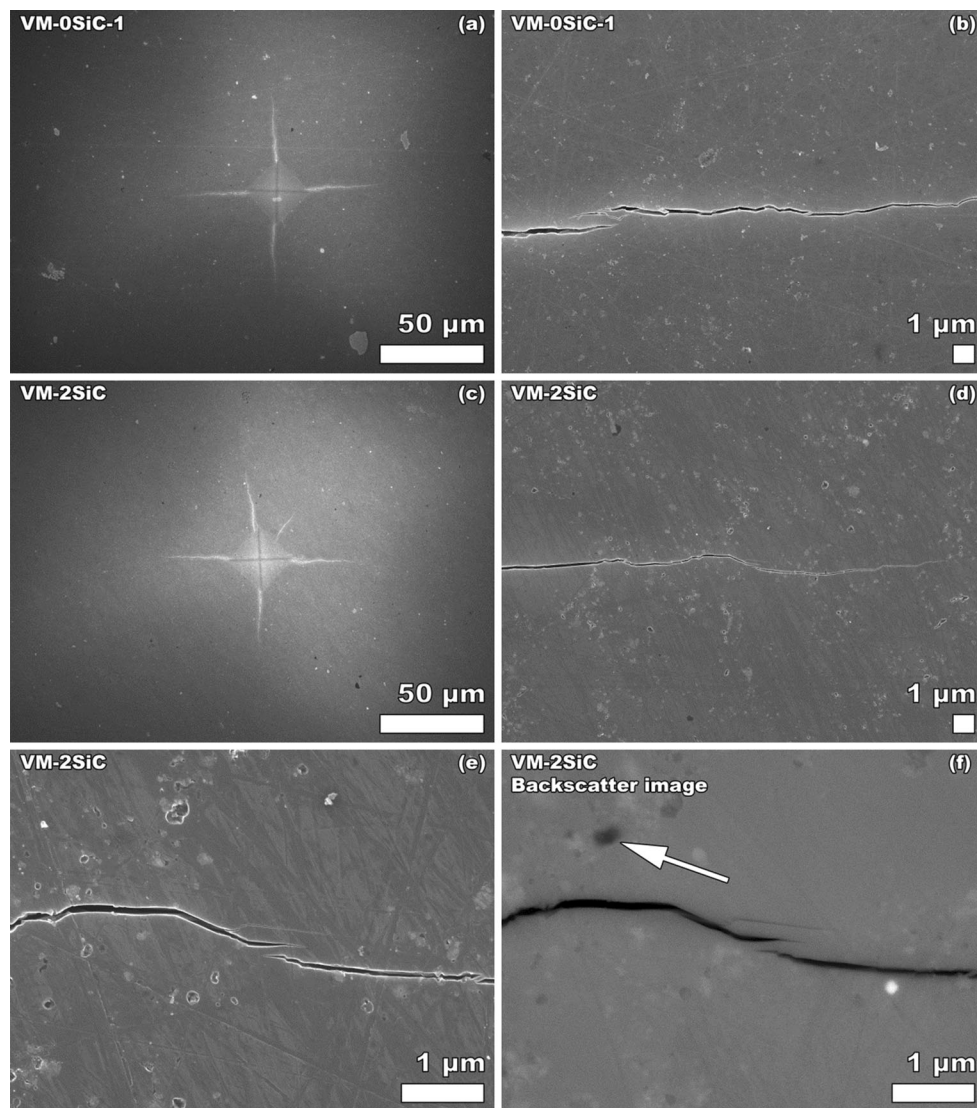


**Fig. 9** Crack bridges were commonly observed in VM specimens regardless of  $\text{SiC}_{\text{NP}}$  addition. Crack bridging in radial cracks in VM specimens without  $\text{SiC}_{\text{NP}}$ , (a) and (b), and in VM  $\text{Mg}_2\text{Si}$  with 2 vol%  $\text{SiC}_{\text{NP}}$ , (c–f), was not eliminated by reducing grain size through VM

processing, although the size of the crack bridges (e) are smaller than those observed in the BM  $\text{Mg}_2\text{Si}$  specimens.  $\text{SiC}_{\text{NP}}$  agglomerates may be seen in backscatter imaging (b), indicated by an arrow

load from 1.96 to 4.9 N, or powder processing technique, averaging 4.8 GPa.

Fracture toughness,  $K_{\text{IC}}$ , of  $\text{Mg}_2\text{Si}$  increases for PM material by 33 % with the addition of 1–2 vol%  $\text{SiC}_{\text{NP}}$ , but  $K_{\text{IC}}$  is independent of  $\text{SiC}_{\text{NP}}$  addition for VM material with up to 2 vol%  $\text{SiC}_{\text{NP}}$ . As is typical of cubic materials such as  $\text{Mg}_2\text{Si}$ ,  $K_{\text{IC}}$  is independent of GS for specimens with no addition of  $\text{SiC}_{\text{NP}}$ . The coefficient of variation for the  $K_{\text{IC}}$  of the VM samples was smaller, 0.08, than for the PM samples, 0.16, indicating a likely smaller scatter of specimen strength for VM specimens than the PM specimens.

**Acknowledgements** The authors acknowledge the financial support of the Department of Energy, Revolutionary Materials for Solid State

Energy Conversion Center, an Energy Frontiers Research Center funded by the U.S. Department of Energy, Office of Science, Office of Basic Energy Sciences under Award number DE-SC0001054.

## References

- Schmidt RD, Case ED, Giles J et al (2012) Room-temperature mechanical properties and slow crack growth behavior of  $\text{Mg}_2\text{Si}$  thermoelectric materials. *J Electron Mater* 41:1210–1216. doi:10.1007/s11664-011-1879-3
- Eilertsen J, Subramanian MA, Kruzic JJ (2013) Fracture toughness of  $\text{Co}_4\text{Sb}_{12}$  and in  $0.1\text{Co}_4\text{Sb}_{12}$  thermoelectric skutterudites evaluated by three methods. *J Alloys Compd* 552:492–498. doi:10.1016/j.jallcom.2012.11.066

3. Ren F, Case ED, Timm EJ, Schock HJ (2008) Hardness as a function of composition for n-type LAST thermoelectric material. *J Alloys Compd* 455:340–345. doi:10.1016/j.jallcom.2007.01.086
4. Ni JE, Case ED, Khahir KN et al (2010) Room temperature Young's modulus, shear modulus, Poisson's ratio and hardness of PbTe–PbS thermoelectric materials. *Mater Sci Eng, B* 170:58–66. doi:10.1016/j.mseb.2010.02.026
5. Wiederhorn SM (1969) Fracture surface energy of glass. *J Am Ceram Soc* 52:99–105. doi:10.1111/j.1151-2916.1969.tb13350.x
6. Launey ME, Ritchie RO (2009) On the fracture toughness of advanced materials. *Adv Mater* 21:2103–2110. doi:10.1002/adma.200803322
7. Foulk JW III, Cannon RRM, Johnson GGC et al (2007) A micromechanical basis for partitioning the evolution of grain bridging in brittle materials. *J Mech Phys Solids* 55:719–743. doi:10.1016/j.jmps.2006.10.009
8. Becher PF (1991) Microstructural design of toughened ceramics. *J Am Ceram Soc* 74:255–269. doi:10.1111/j.1151-2916.1991.tb06872.x
9. Ritchie R (1999) Mechanisms of fatigue-crack propagation in ductile and brittle solids. *Int J Fract* 100:55–83. doi:10.1023/A:1018655917051
10. Case ED (2012) Thermo-mechanical properties of thermoelectric materials. In: Rowe DM (ed) thermoelectrics and its energy harvesting, modules, systems, and applications. CRC Press, Boca Raton, p 581
11. Case ED (2012) Thermal fatigue and waste heat recovery via thermoelectrics. *J Electron Mater* 41:1811–1819. doi:10.1007/s11664-012-2083-9
12. Lathabai S, Rodel J, Lawn BR (1991) Cyclic fatigue from frictional degradation at bridging grains in alumina. *J Am Ceram Soc* 74:1340–1348. doi:10.1111/j.1151-2916.1991.tb04109.x
13. Bhowmick S, Meléndez-Martínez JJ, Lawn BR (2007) Bulk silicon is susceptible to fatigue. *Appl Phys Lett* 91:201902. doi:10.1063/1.2801390
14. Bhowmick S, Cha H, Jung Y-G, Lawn BR (2009) Fatigue and debris generation at indentation-induced cracks in silicon. *Acta Mater* 57:582–589. doi:10.1016/j.actamat.2008.10.006
15. Knehans R, Steinbrech R (1982) Memory effect of crack resistance during slow crack growth in notched Al<sub>2</sub>O<sub>3</sub> bend specimens. *J Mater Sci Lett* 1:327–329. doi:10.1007/BF00726477
16. Pérez-Rigueiro J, Pastor J, Llorca J et al (1998) Revisiting the mechanical behavior of alumina/silicon carbide nanocomposites. *Acta Mater* 46:5399–5411. doi:10.1016/S1359-6454(98)00193-1
17. Parchovianský M, Galusek D, Sedláček J et al (2013) Microstructure and mechanical properties of hot pressed Al<sub>2</sub>O<sub>3</sub>/SiC nanocomposites. *J Eur Ceram Soc* 33:2291–2298. doi:10.1016/j.jeurceramsoc.2013.01.024
18. Zhao L-D, Zhang B-P, Li J-F et al (2008) Thermoelectric and mechanical properties of nano-SiC-dispersed Bi<sub>2</sub>Te<sub>3</sub> fabricated by mechanical alloying and spark plasma sintering. *J Alloys Compd* 455:259–264. doi:10.1016/j.jallcom.2007.01.015
19. Tani J, Kido H (2005) Thermoelectric properties of bi-doped MgSi semiconductors. *Phys B Condens Matter* 364:218–224. doi:10.1016/j.physb.2005.04.017
20. Hayatsu Y, Iida T, Sakamoto T et al (2012) Fabrication of large sintered pellets of Sb-doped n-type Mg<sub>2</sub>Si using a plasma activated sintering method. *J Solid State Chem* 193:161–165. doi:10.1016/j.jssc.2012.07.008
21. Tani J, Kido H (2008) Thermoelectric properties of Al-doped Mg<sub>2</sub>Si<sub>1-x</sub>Sn<sub>x</sub> (x ≤ 0.1). *J Alloys Compd* 466:335–340. doi:10.1016/j.jallcom.2007.11.029
22. Meng QS, Fan WH, Chen RX, Munir ZA (2011) Thermoelectric properties of Sc- and Y-doped Mg<sub>2</sub>Si prepared by field-activated and pressure-assisted reactive sintering. *J Alloys Compd* 509:7922–7926. doi:10.1016/j.jallcom.2011.05.033
23. Muthiah S, Pulikkotil J, Srivastava AK et al (2013) Conducting grain boundaries enhancing thermoelectric performance in doped Mg<sub>2</sub>Si. *Appl Phys Lett* 103:053901. doi:10.1063/1.4816802
24. Tani J, Kido H (2007) Thermoelectric properties of Sb-doped Mg<sub>2</sub>Si semiconductors. *Intermetallics* 15:1202–1207. doi:10.1016/j.intermet.2007.02.009
25. Li J-F, Liu J (2006) Effect of nano-SiC dispersion on thermoelectric properties of Bi<sub>2</sub>Te<sub>3</sub> polycrystals. *Phys Status Solidi* 203:3768–3773. doi:10.1002/pssa.200622011
26. Li J, Tan Q, Li J-F et al (2013) BiSbTe-based nanocomposites with high ZT: the effect of SiC nanodispersion on thermoelectric properties. *Adv Funct Mater* 23:4317–4323. doi:10.1002/adfm.201300146
27. Li Z-Y, Li J-F, Zhao W-Y et al (2014) PbTe-based thermoelectric nanocomposites with reduced thermal conductivity by SiC nanodispersion. *Appl Phys Lett* 104:113905. doi:10.1063/1.4869220
28. Alfa-Aesar material safety data sheet, magnesium silicide. <http://www.alfa.com/content/msds/USA/45518.pdf>
29. Pilchak AL, Ren F, Case ED et al (2007) Characterization of dry milled powders of LAST (lead–antimony–silver–tellurium) thermoelectric material. *Philos Mag* 87:4567–4591. doi:10.1080/14786430701566044
30. Schreiber E, Soga N (1966) Elastic constants of silicon carbide. *J Am Ceram Soc* 49:342. doi:10.1111/j.1151-2916.1966.tb13278.x
31. Schmidt RD, Ni JE, Case ED et al (2010) Room temperature Young's modulus, shear modulus, and Poisson's ratio of Ce<sub>0.9</sub>Fe<sub>3.5</sub>Co<sub>0.5</sub>Sb<sub>12</sub> and Co<sub>0.95</sub>Pd<sub>0.05</sub>Te<sub>0.05</sub>Sb<sub>3</sub> skutterudite materials. *J Alloys Compd* 504:303–309. doi:10.1016/j.jallcom.2010.06.003
32. Migliori A, Sarrao JL (1997) Resonant ultrasound spectroscopy: applications to physics, materials measurements, and nondestructive evaluation. Wiley, New York
33. Wachtman JB, Cannon WR, Mathewson MJ (2009) Mechanical properties of ceramics, 2nd edn. Wiley, Hoboken
34. ASTM-Standard-E112-13 (2014) Standard test methods for determining average grain size. ASTM Vol 0301 Met Mech Testing; Elev Low Temp Tests; Metallogr. doi: 10.1520/E0112-13
35. Whitten W, Chung P, Danielson G (1965) Elastic constants and lattice vibration frequencies of Mg<sub>2</sub>Si. *J Phys Chem Solids* 26:49–56. doi:10.1016/0022-3697(65)90071-5
36. Durand MA (1936) The temperature variation of the elastic moduli of NaCl, KCl and MgO. *Phys Rev* 50:449–455. doi:10.1103/PhysRev.50.449
37. Schmidt RD, Case ED, Ni JE et al (2013) High-temperature elastic moduli of thermoelectric SnTe<sub>1-x</sub>Si<sub>x</sub> nanoparticulate composites. *J Mater Sci* 48:8244–8258. doi:10.1007/s10853-013-7637-6
38. Hashin Z (1962) The elastic moduli of heterogeneous materials. *J Appl Mech* 29:143–150. doi:10.1115/1.3636446
39. Bedolla E, Lemus-Ruiz J, Contreras A (2012) Synthesis and characterization of Mg-AZ91/AlN composites. *Mater Des* 38:91–98. doi:10.1016/j.matdes.2012.02.001
40. Couturier R, Ducret D, Merle P et al (1997) Elaboration and characterization of a metal matrix composite: Al/AlN. *J Eur Ceram Soc* 17:1861–1866
41. Carnahan RD (1968) Elastic properties of silicon carbide. *J Am Ceram Soc* 51:223–224. doi:10.1111/j.1151-2916.1968.tb11877.x
42. Rice RW (1998) Porosity of Ceramics. Marcel Dekker, New York
43. Anderson OL, Andreatch P (1966) Pressure derivatives of elastic constants of single-crystal MgO at 23° and –195.8°C. *J Am Ceram Soc* 49:404–409. doi:10.1111/j.1151-2916.1966.tb15405.x
44. Bogardus EH (1965) Third-order elastic constants of Ge, MgO, and fused SiO<sub>2</sub>. *J Appl Phys* 36:2504. doi:10.1063/1.1714520
45. Simmons G, Wang H (1971) Single crystal elastic constants and calculated aggregate properties: a handbook, 2nd edn. Press, Cambridge, Massachusetts, The M.I.T

46. Schmidt RD, Case ED, Lehr GJ, Morelli DT (2013) Room temperature mechanical properties of polycrystalline  $\text{YbAl}_3$ , a promising low temperature thermoelectric material. *Intermetallics* 35:15–24. doi:[10.1016/j.intermet.2012.11.019](https://doi.org/10.1016/j.intermet.2012.11.019)
47. Ni JE, Ren F, Case ED, Timm EJ (2009) Porosity dependence of elastic moduli in LAST (Lead–antimony–silver–tellurium) thermoelectric materials. *Mater Chem Phys* 118:459–466. doi:[10.1016/j.matchemphys.2009.08.018](https://doi.org/10.1016/j.matchemphys.2009.08.018)